Geophysical Research Letters

RESEARCH LETTER
10.1029/2025GL118168

Wave Heating of Magnetotail Current Sheet Electrons at Mars

Liang Yu[1,2,3], Zhenpeng Su[1,2,3,4], Sanwei Cheng[1,2,3], Zhiyong Wu[1,2,3], Zewen Chen[1,2,3], Zhaojin Rong[5,6,7], and Yuming Wang[1,2,3]

[1]National Key Laboratory of Deep Space Exploration/School of Earth and Space Sciences, University of Science and Technology of China, Hefei, China, [2]CAS Center for Excellence in Comparative Planetology/CAS Key Laboratory of Geospace Environment/Mengcheng National Geophysical Observatory, University of Science and Technology of China, Hefei, China, [3]Collaborative Innovation Center of Astronautical Science and Technology, Harbin, China, [4]State Key Laboratory of Lunar and Planetary Sciences, Macau University of Science and Technology, Macao, China, [5]Key Laboratory of Planetary Science and Frontier Technology, Institute of Geology and Geophysics, Chinese Academy of Sciences, Beijing, China, [6]College of Earth and Planetary Sciences, University of Chinese Academy of Sciences, Beijing, China, [7]Mohe Observatory of Geophysics, Beijing National Observatory of Space Environment, Institute of Geology and Geophysics, Chinese Academy of Sciences, Beijing, China

Key Points:

- The thermal pressure of electrons within the Martian magnetotail current sheet can effectively balance the external magnetic pressure
- The electron population, likely sourced from both ionosphere and magnetosheath, shapes thermal and kinetic properties of the current sheet
- Magnetosonic, whistler, and electron cyclotron harmonic waves can heat electrons, whether driven externally or generated internally

Supporting Information:

Supporting Information may be found in the online version of this article.

Correspondence to:

Z. Su,
szpe@mail.ustc.edu.cn

Citation:

Yu, L., Su, Z., Cheng, S., Wu, Z., Chen, Z., Rong, Z., & Wang, Y. (2025). Wave heating of magnetotail current sheet electrons at Mars. *Geophysical Research Letters*, *52*, e2025GL118168. https://doi.org/10.1029/2025GL118168

Received 17 JUL 2025
Accepted 5 NOV 2025

Abstract The Martian magnetotail current sheet serves as a critical pathway for ionospheric ion escape. Contrary to the conventional view that external magnetic pressure is balanced mainly by internal ion thermal pressure, we present novel observations from the Mars Atmosphere and Volatile Evolution spacecraft of an electron-dominated pressure balance configuration. The current sheet electrons exhibit two distinct populations: a thermal core of ionospheric origin and a suprathermal shell of magnetosheath origin. Their bulk temperature reaches up to three times higher than that outside the current sheet. Based on linear instability analysis, we propose two candidate heating mechanisms: (a) Landau resonant or transit-time heating by magnetosonic waves likely originating from the magnetosheath, and (b) Landau or cyclotron resonant heating by whistler and electron cyclotron harmonic waves generated spontaneously from the shell-like electron velocity distribution. These results highlight the potentially significant role of plasma waves in sustaining the Martian atmospheric escape channels.

Plain Language Summary Mars does not have a global magnetic field like Earth, but it still forms a "magnetotail"—an extended region behind the planet shaped by the Sun's magnetic field. A thin layer in this magnetotail, called the current sheet, plays a key role in allowing charged particles from Mars' upper atmosphere to escape into space. While earlier studies suggested that ion thermal pressure typically supports the force balance in this region, our observations from NASA's MAVEN spacecraft data reveal a distinct type of current sheet in which the pressure balance is dominated by electrons rather than ions. We find that electrons inside these current sheets are significantly hotter than those measured outside. Our detailed analysis supports two possible heating mechanisms: one involving magnetosonic waves coming from the surrounding space environment, and another driven by whistler and electron cyclotron harmonic waves generated internally. These findings highlight the important role of plasma waves in sustaining the Martian atmospheric escape channels.

1. Introduction

In terrestrial planetary systems, magnetotail current sheets serve as important pathways for the escape of atmospheric constituents into space. For Earth, the magnetotail current sheet is primarily formed by the stretching of the intrinsic magnetic field on the nightside (L. Zelenyi et al., 2019). Within this current sheet, $J \times B$ acceleration and plasmoid ejection associated with magnetic reconnection facilitate the escape of oxygen ions (Ieda et al., 1998). Oxygen ion escape through the magnetotail current sheet is estimated to account for approximately 40% of the global loss (Seki et al., 2001). In contrast, planets such as Mars and Venus, which lack a global intrinsic magnetic field, develop their magnetotail current sheets mainly through the draping and subsequent stretching of interplanetary magnetic fields on the nightside (e.g., Dubinin & Fraenz, 2015; Dubinin et al., 2019; L. Zelenyi et al., 2019). The $J \times B$ acceleration within these induced current sheets contributes to up to 70% of the total oxygen ion loss (e.g., Barabash, Fedorov, Lundin, & Sauvaud, 2007; Barabash, Fedorov, Sauvaud, et al., 2007; Dubinin et al., 2017; Fedorov et al., 2008, 2011; Jakosky, Grebowsky, et al., 2015; Nilsson et al., 2023; Zhang et al., 2024).

A fundamental scientific question concerns how these magnetotail current sheets maintain force balance. In classical current sheet models (e.g., Harris, 1962; Artemyev, Vasko, et al., 2016; L. M. Zelenyi et al., 2022), the external magnetic pressure is balanced by the internal thermal pressure of particles. At Earth, ion thermal pressure statistically dominates over electron thermal pressure (e.g., Artemyev, Angelopoulos, & Runov, 2016; Artemyev et al., 2019). The ion-to-electron temperature ratio typically ranges from 3 to 4 and can reach as high as 15 in extreme cases (Artemyev, Angelopoulos, & Runov, 2016). Several potential heating mechanisms for current sheet particles have been proposed, including adiabatic heating during earthward convection (e.g., Artemyev et al., 2012; Baumjohann, 1998), slow-mode shock heating associated with magnetotail reconnection (Baumjohann, 1998), Landau, transit-time, and stochastic heating by kinetic Alfvén waves (Chaston et al., 2014), and Landau heating by quasi-monochromatic magnetosonic waves (Tsurutani & Smith, 1984). At Mars, the importance of internal ion thermal pressure in maintaining the balance of the magnetotail current sheet has been widely investigated (e.g., Artemyev et al., 2017; DiBraccio et al., 2015; Harada et al., 2015; Li et al., 2023; Zhang et al., 2024). Although enhanced electron fluxes in the current sheet have long been observed (e.g., Halekas et al., 2006; Halekas et al., 2008; Xu et al., 2024; Zhang et al., 2025), the potential significance of electron thermal pressure and the underlying heating mechanisms remain largely unexplored.

In this Letter, we report observations by the Mars Atmosphere and Volatile Evolution (MAVEN) spacecraft (Jakosky, Lin, et al., 2015) of Martian magnetotail current sheets in which the external magnetic pressure was predominantly balanced by the thermal pressure of electrons rather than ions. Based on the observational data and linear instability analysis, we propose two plausible electron heating mechanisms: one driven by externally originated magnetosonic waves, and the other by spontaneously generated whistler and electron cyclotron harmonic (ECH) waves.

2. Data and Instrumentation

We utilize data from three instruments aboard the MAVEN spacecraft: the magnetometer (MAG) (Connerney et al., 2015), the Supra-Thermal And Thermal Ion Composition (STATIC) experiment (McFadden et al., 2015), and the Solar Wind Electron Analyzer (SWEA) (Mitchell et al., 2016). MAG provides magnetic field vector data at both 1 and 32 Hz cadences. We use the 1 Hz data, which are sufficient to resolve the quasi-periodic magnetosonic oscillations under investigation. STATIC measures ion composition and velocity distributions from 0.1 eV to 30 keV. We identify ion species by mass-to-charge ratio (in units of atomic mass per elementary charge) (Fowler et al., 2022): H^+ (0–1.55), He^{++} or H_2^+ (1.55–2.7), O^+ (14–20), O_2^+ (20–40), and CO_2^+ (40–60). We calculate these ion moments using the same algorithm as in the Space Physics Environment Data Analysis System (SPEDAS) (Angelopoulos et al., 2019), with corrections for spacecraft velocity and potential. However, due to the finite mass resolution of STATIC, CO_2^+ measurements may be contaminated by O_2^+ ions of similar mass (Text S1 and Figures S1 and S2 in Supporting Information S1). SWEA measures electron velocity distributions from 3 to 4600 eV. We apply the correction algorithm implemented by Andreone et al. (2022) in the SPEDAS to remove spacecraft photoelectron and secondary electron contamination, and then compute the electron moments from the corrected distributions (Text S2 and Figure S3 in Supporting Information S1).

3. Event Overview

Around 00:47 UT on 19 February 2018, MAVEN crossed the magnetotail current sheet, identified by a reversal in the x-component of the magnetic field in the Mars Solar Orbital (MSO) coordinate system (Figures 1a–1d). This event was included in a statistical survey investigating the influence of the radial interplanetary magnetic field component on the magnetotail current sheet structure (Wen et al., 2025). Across the transition, the magnetic field strength decreased (Figures 1d and 1e), while particle densities and temperatures increased (Figures 1f and 1h). The ion population shifted toward heavier species (Figure 1f), which exhibited very low temperatures (Figure 1h and Figure S1 in Supporting Information S1). The external magnetic pressure $P_{\mathrm{B}} = \frac{B^2}{2\mu_0}$ was largely balanced by the internal electron thermal pressure $P_{\mathrm{e}} = n_e k_{\mathrm{B}} T_e$. While both density and temperature contributed to the enhanced electron thermal pressure, the factor-of-three increase in electron temperature (from 15 eV outside to 45 eV inside the current sheet) represented a significant input of thermal energy.

The current sheet electrons exhibited two distinct populations: a thermal core and a suprathermal shell, separated by a pronounced dip in phase space density (PSD) at intermediate energies (Figures 2a and 2b). The thermal core likely originated from dayside ionospheric plasma transported across the terminator or from nightside

10.1029/2025GL118168

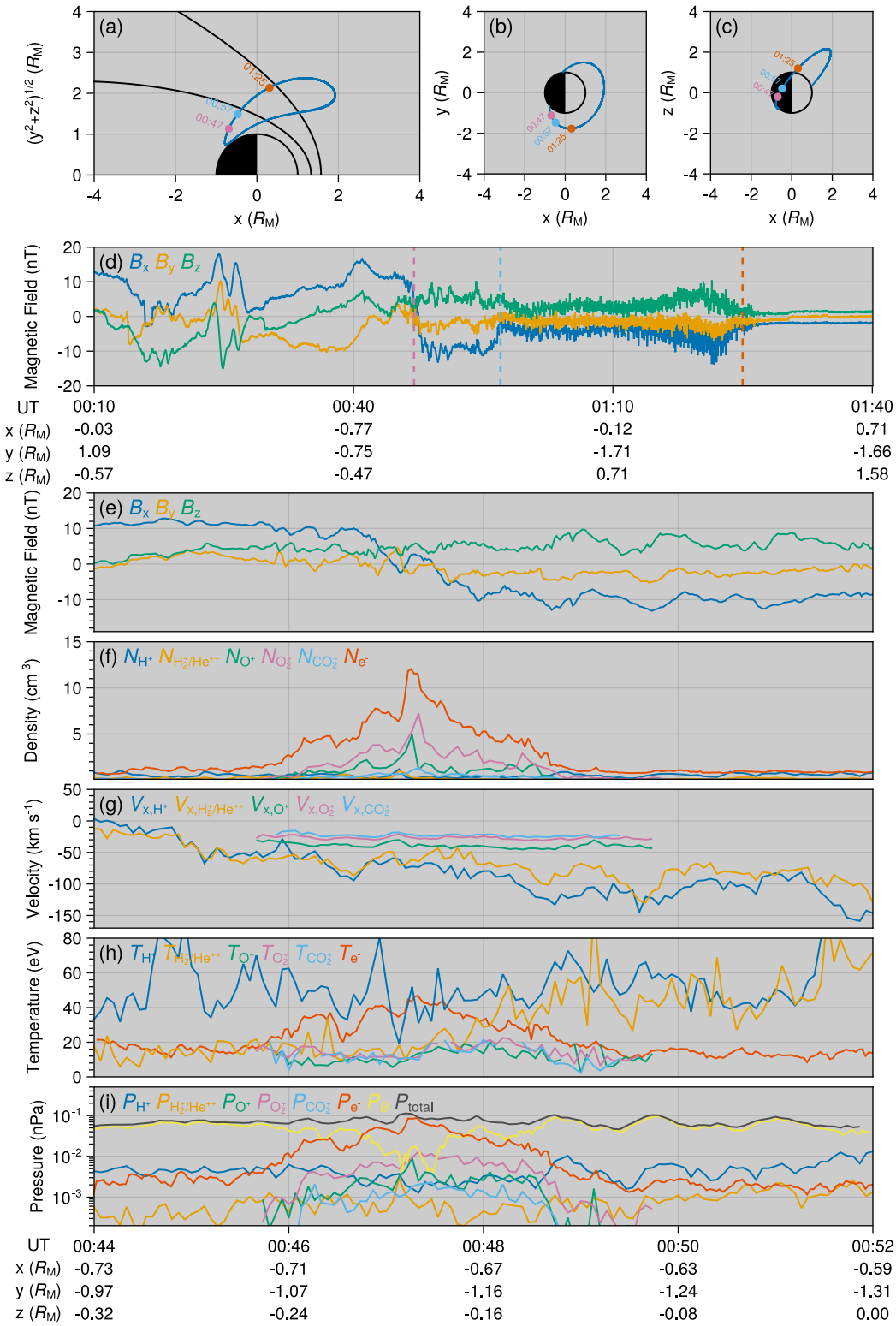

Figure 1.

atmospheric ionization induced by precipitating electrons (Fox et al., 1993). The suprathermal shell, peaking near ~30 eV and extending smoothly beyond 100 eV, likely originated in the magnetosheath and underwent subsequent acceleration and heating. We define "acceleration" as bulk energy gain and "heating" as enhanced random thermal motion. Acceleration may be attributed to the ambipolar electrostatic potential proposed by Xu et al. (2024), while the heating mechanism is the focus of this study. Both electron populations were nearly isotropic (Figure 2c), indicating effective thermalization. In contrast, outside the current sheet, suprathermal electrons (>5 eV) displayed significant anisotropy (Figures 2e and 2f). For the subsequent theoretical analysis, we model the observed PSD as a superposition of multiple generalized Maxwellian ring-beam distributions (Figures 2d and 2g, Text S3 and Table S1 in Supporting Information S1), a functional form similar to that used in previous studies of Martian magnetosheath ion populations (e.g., Halekas et al., 2023; Shen et al., 2025).

4. Wave-Driven Heating of Electrons

4.1. Magnetosonic Waves Originating Externally

Quasi-periodic magnetic field perturbations extending from the magnetosheath-side to the center of the current sheet (Figures 3a and 3b) suggest that electron heating by externally originated waves is a plausible mechanism. To isolate wave signals from the background field, we apply a zero-phase, fourth-order, low-pass Butterworth filter with a cutoff frequency of 0.01 Hz to the magnetic field data (Text S4 and Figure S4 in Supporting Information S1). We apply Minimum Variance Analysis (MVA) (Sonnerup & Scheible, 1998) to the background magnetic field and determine the current sheet normal as the direction of minimum variance (Figure 3a and Text S5 in Supporting Information S1). Similarly, we apply MVA to the filtered wave fields and identify the wave vector direction as the minimum variance direction, with a 180° ambiguity (Text S5 and Figure S5 in Supporting Information S1). On the magnetosheath-side (00:49–00:50 UT) of the current sheet, we determine the wave normal angle ψ to be either 80° or 100°. We estimate the corresponding wave frequency in the spacecraft frame as $\omega_{\rm obs} = 0.105\,{\rm rad}\cdot{\rm s}^{-1}$ by averaging the intervals between adjacent peaks in the filtered magnetic field component (Figure 3b). The low frequency, quasi-perpendicular propagation, and strong in-phase correlation between magnetic and thermal pressure fluctuations (Figure 1i) collectively confirm the magnetosonic nature of these waves.

We compute the hot plasma wave dispersion relations (Figure 3c) using the BO code (e.g., Xie, 2019; Xie & Xiao, 2016) with representative plasma parameters outside the current sheet (Table S1 in Supporting Information S1). The magnetosonic wave dispersion is well approximated by $\omega = kV_{\rm A}$, and the Poynting flux is estimated as $S = V_{\rm A}|\Delta\mathbf{B}|^2/(4\mu_0)$, where $\Delta\mathbf{B}$ is the wave magnetic amplitude. From the magnetosheath-side (00:49–00:50 UT) to the center (00:47 UT), $V_{\rm A}$ decreased by a factor of ~21, while $|\Delta\mathbf{B}|$ remained nearly constant. Under the assumption of steady-state wave energy transport, this implies a net inward energy flux, which is only consistent with waves incident toward the current sheet at a wave normal angle of ~80°.

To determine the wave frequency ω and wave vector $\mathbf{k}$ in the plasma rest frame, we simultaneously solve the hot plasma dispersion relation (Figure 3c) and the Doppler shift equation

$$\omega_{\rm obs} = \mathbf{k}\cdot\mathbf{V} + \omega, \tag{1}$$

where $\mathbf{V} \approx (34.5, 6.5, 0.5)\ {\rm km}\cdot{\rm s}^{-1}$ denotes the velocity of the spacecraft relative to the plasma (Fowler et al., 2021). Among the multiple solutions, only one exhibits wave polarization consistent with the observations (Figures 3d and 3e), which we identify as the physical mode with $\omega = 0.132\,{\rm rad}\cdot{\rm s}^{-1}$ and $\mathbf{k} = (-1.13, 1.81, 0.09) \times 10^{-3}\ {\rm km}^{-1}$. Polarization analysis is performed in a mean-field-aligned (MFA) coordinate system, with $\mathbf{e}_{\parallel}$

Figure 1. Overview of the current sheet properties observed on 19 February 2018. (a–c) MAVEN trajectory in the Mars Solar Orbital (MSO) coordinate system, with three markers indicating the locations of the current sheet, the outer boundary of the induced magnetosphere, and the bow shock. (d) Magnetic field from the induced magnetosphere through the magnetosheath to the upstream solar wind. (e–i) Magnetic field and plasma properties near the current sheet: (e) Magnetic field; (f) Electron and ion number densities; (g) Ion velocities along the x-direction in the MSO coordinate system; (h) Electron and ion temperatures; (i) Thermal pressures of ions and electrons, magnetic pressure, and total pressure. In each panel, colors help distinguish the indicated quantities. Heavy ion data in panels (g–h) are shown only during 00:45:44–00:48:48 UT, when densities are high enough for reliable detection. These data have been filtered to remove outliers exceeding three times the local variation.

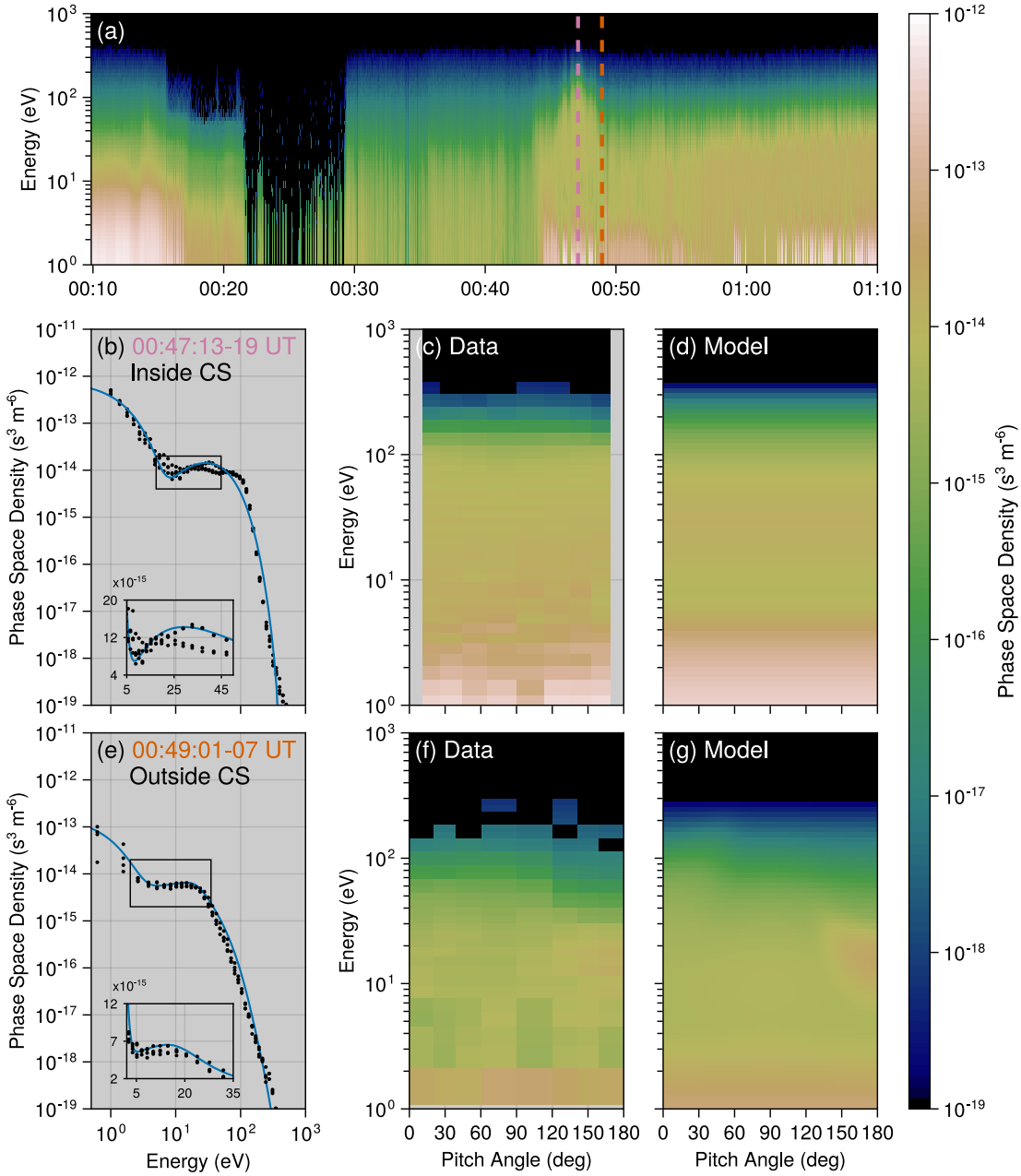

Figure 2. Observed and modeled electron PSDs on 19 February 2018. (a) Spatiotemporal evolution of electron PSDs, with two dashed lines indicating the time moments analyzed in the subsequent panels. Electron PSDs (b–d) inside and (e–g) outside the current sheet. (b, e) Energy dependence of angle-averaged electron PSDs, with inset panels highlighting the transition between two electron populations. Solid dots represent observations at four adjacent time moments, and solid lines represent the modeling results. (c, f) Observed and (d, g) modeled electron PSDs as functions of energy and pitch angle.

along the background magnetic field, $\mathbf{e}_{\perp 1}$ in the direction of $\mathbf{e}_{\parallel} \times \mathbf{k}$, and $\mathbf{e}_{\perp 2} = \mathbf{e}_{\perp 1} \times \mathbf{e}_{\parallel}$ completing the orthogonal triad.

By analogy with ionospheric plasma heating by magnetosonic waves (e.g., Fowler et al., 2018; Fowler et al., 2020; Su et al., 2020), the observed magnetosonic wave is expected to propagate into the current sheet and heat the plasma therein. In the plasma rest frame, the linear wave-particle resonance condition is given by

$$\omega - k_{\parallel} v_{\parallel} = n\Omega_s, \tag{2}$$

10.1029/2025GL118168

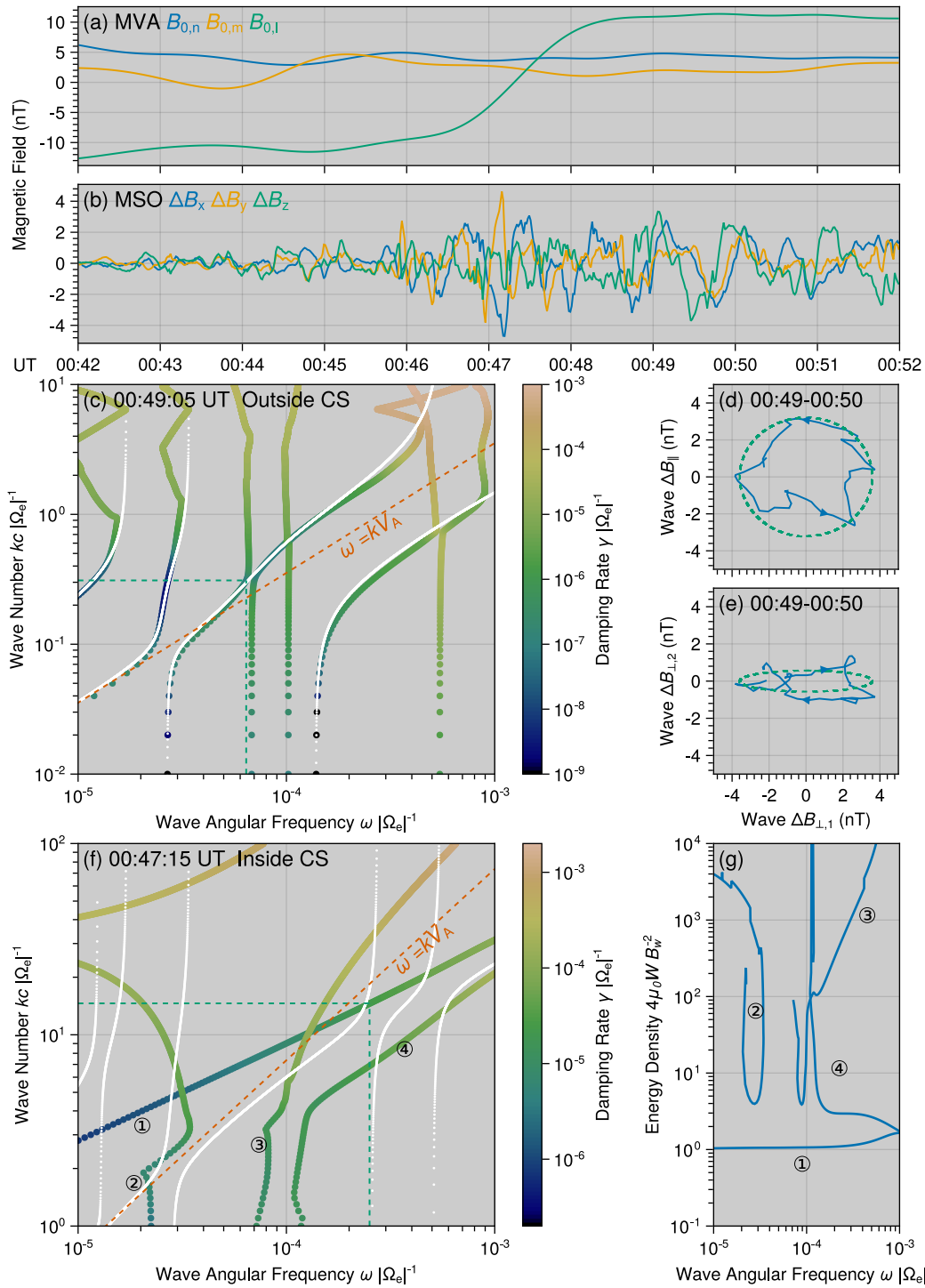

Figure 3. Magnetosonic waves inside and outside the current sheet. (a) Background magnetic field in the MVA coordinate system. (b) Wave magnetic field in the MSO coordinate system. (c) Comparison between the cold plasma dispersion relation (white dots) and the hot plasma dispersion relation (color-coded according to damping rate) outside the current sheet. The orange dashed line represents the dispersion relation of $\omega = kV_A$. The dashed lines indicate specific wavenumbers and frequencies in the local plasma frame. (d and e) Comparison of magnetic polarizations between observations (solid lines) and predictions from hot plasma wave theory in the MFA coordinate system. Arrows indicate the rotation direction of the magnetic field vector. (f) Same as panel (c), but for analysis inside the current sheet. (g) Hot plasma wave energy density. The first wave mode corresponds to the magnetosonic wave, while the other wave modes may represent coupled modes between ion Bernstein modes and acoustic modes (with particle kinetic energies much greater than wave magnetic energies).

where $k_{\parallel} = |\mathbf{k}|\cos\psi$ is the component of the wave vector parallel to the background magnetic field, n is the resonance order, and $\Omega_s = q_s B/m_s$ is the gyrofrequency of the sth particle species. As derived by (Summers et al., 2007), the minimum kinetic energy required for a particle to resonate with the wave is

$$E_{\min} = \frac{1}{2} m_s \left(\frac{\omega - n\Omega_s}{k_{\parallel}} \right)^2, \tag{3}$$

with wave parameters obtained from BO solution using representative current sheet plasma conditions (Table S1 in Supporting Information S1). For e^- and H^+, the minimum resonant energy occurs at the $n = 0$ Landau resonance. Because the wave frequency is close to the gyrofrequency of H_2^+, the minimum resonant energies of H_2^+, O^+, O_2^+, and CO_2^+ occur at the $n = 1, 8, 16$, and 22 cyclotron resonances, respectively. The minimum Landau resonant energy for e^- is 2.53×10^{-3} eV, several orders of magnitude below their thermal energy, indicating strong electron Landau damping. For H^+ and H_2^+, the minimum resonant energies (4.64 and 0.06 eV) are also below their thermal energies, but their low number densities limit damping contributions. Although the minimum resonant energies of O^+, O_2^+, and CO_2^+ are low compared to their thermal energies, the high resonance orders result in weak wave-particle coupling. The first-order ($n = 1$) resonant energies for O^+, O_2^+, and CO_2^+ are 55.5 eV, 129.0 eV, and 184.4 eV, respectively, several times higher than their thermal energies. These results indicate that ion resonant damping is negligible compared to electron Landau damping within the current sheet.

According to linear theory (e.g., Shklyar, 2017; Stix, 1992), the rate of change of the particle kinetic energy density P_{WP} is given by

$$P_{WP} = 2\gamma W, \tag{4}$$

where γ is the wave damping rate and W is the total electromagnetic and acoustic energy density of the wave. The BO solution inside the current sheet yields $\gamma = 1.27 \times 10^{-2}\ s^{-1}$ (Figure 3f). The absence of direct electric-field measurements prevents a direct evaluation of the full Poynting flux. Assuming a constant wave Poynting flux across the current sheet boundary, a combination of BO solutions inside and outside the current sheet gives $W = 7.41 \times 10^{-11}\ J \cdot m^{-3}$ (Figure 3g). This results in an estimated energy deposition rate of $P_{WP} \approx 11.8\ eV \cdot cm^{-3} \cdot s^{-1}$. By analogy with studies in Earth's inner magnetosphere (Wu et al., 2023) and within idealized magnetohydrodynamic frameworks (Núñez, 2020), magnetosonic waves incident on the current sheet may experience partial reflection or mode conversion. Reflection reduces the net energy deposition, while mode conversion can alter heating efficiency depending on the nature of the resulting wave modes. The current sheet exhibits strong inhomogeneity, with a thickness (~600 km) much smaller than the magnetosonic wavelength (~2900 km), violating the uniformity requirement for Landau damping. Thus, the dominant mechanism is better characterized as transit-time damping (e.g., Robinson, 1989; Robinson, 1991), due to particles crossing the confined wave field. Qualitatively, higher Landau damping rates generally correspond to lower transit-time damping rates (Short & Simon, 1998). Despite these limitations, our estimate provides a first-order approximation for the upper bound of electron heating within the current sheet.

4.2. Whistler and ECH Waves Generated Spontaneously

Electron pressure–sustained current sheets in the Martian magnetotail are not rare, yet magnetosonic waves are not always observed (Figures S9–S11 in Supporting Information S1). Instead, the shell-like electron distribution can spontaneously generate whistler, ECH, upper hybrid, and RX-mode waves (Sundkvist et al., 2006; Tataronis & Crawford, 1970; Umeda et al., 2012), due to a positive energy gradient in the electron PSD. We systematically evaluated these wave modes and identified the two most unstable inside the current sheet: whistler and ECH waves (Figure 4a). For whistler waves, the growth rate peaks at a wave normal angle near 77° (Figure 4b), with energy transfer via Landau resonance (Figure 4c). ECH modes, in contrast, show maximum growth around 89°, extracting energy through harmonic cyclotron resonances (Figure 4c). The substantial growth rates on the order of $10^0\ s^{-1}$ for both modes suggest rapid wave growth, which would effectively flatten the PSD energy gradient and lead to electron heating. However, the magnetic field data, with a sampling rate up to 32 Hz, lacked the temporal resolution needed to fully resolve whistler waves, and no high-frequency electric field data were available for direct ECH wave analysis.

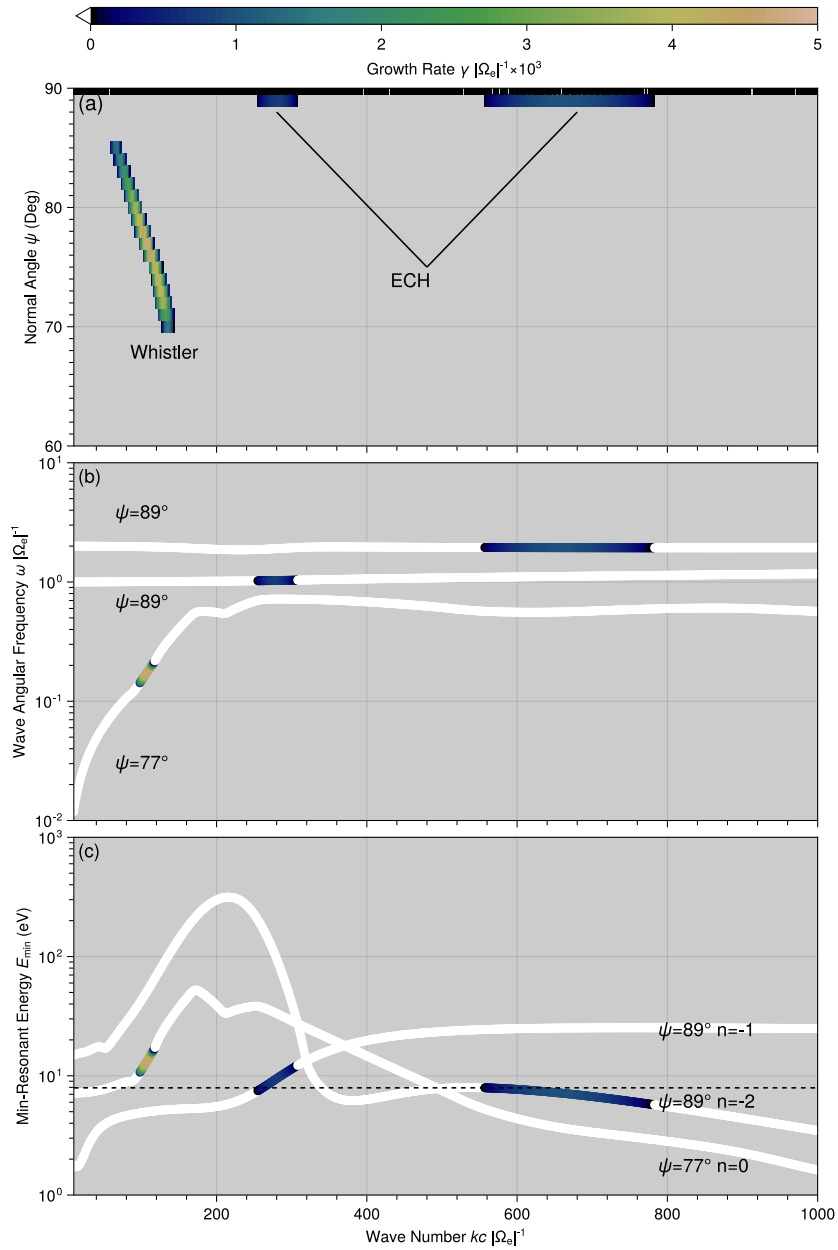

Figure 4. Linear instability analysis of the observed electron distribution inside the current sheet. (a) Maximum wave growth rate over all frequencies, shown as a function of wavenumber and wave normal angle. (b) Dispersion relations of the dominant unstable modes, identified as whistler and ECH waves, with wave normal angles selected to maximize growth. (c) Minimum resonant energies for the identified waves at various resonance orders. The dashed line marks the energy of the observed PSD dip. Colors in all panels represent the growth rates.

5. Summary and Discussion

We report novel MAVEN observations of a distinct Martian magnetotail current sheet in which the external magnetic pressure is balanced primarily by the internal thermal pressure of electrons. From outside to inside the current sheet, the bulk electron temperature increases by up to a factor of three, reaching values up to five times higher than those of heavy ions. The electron velocity distribution within the current sheet consists of two components: a thermal core, likely originating from the ionosphere, and a suprathermal shell, likely originating from the magnetosheath (Xu et al., 2024). Based on linear instability analysis, we propose two candidate heating mechanisms:

1. Landau resonant or transit-time heating by magnetosonic waves, potentially driven by foreshock ultralow frequency waves in the induced magnetosphere (e.g., Brain et al., 2002; Collinson et al., 2018; Fowler et al., 2018, 2020; Ruhunusiri et al., 2015; Su et al., 2020, 2023). The estimated electron Landau heating rate by magnetosonic waves reaches up to 11.8 $eV \cdot cm^{-3} \cdot s^{-1}$. However, this estimate is subject to uncertainties due to the lack of direct electric field measurements, unmodeled wave reflection and mode conversion, and the omission of transit-time damping in the finite-scale current sheet. More accurate quantification will require future coordinated electromagnetic observations and high-resolution kinetic simulations.
2. Landau and cyclotron resonant heating mediated by whistler and ECH waves, which are self-consistently generated by the shell-type electron velocity distribution. These waves can grow rapidly under the observed conditions, with a peak growth rate on the order of 10^0 s^{-1}, and are expected to scatter electrons via Landau and cyclotron resonances, thereby flattening the initially positive gradient in PSD along the energy direction. This process results in a net transfer of free energy from the unstable electron population to thermal motion, manifesting as a significant increase in electron temperature. This evolution is analogous to the saturation of the Bernstein instability in Earth's magnetospheric plasmas with partial-shell electron distributions (Umeda et al., 2007) or shell-like ion distributions (Liu et al., 2011), where wave-particle interactions drive the system toward a quasi-steady, heated state. The pre-relaxed electron distribution could have been more anisotropic than observed, providing stronger free energy sources for wave growth (Text S6 and Figures S6 and S7 in Supporting Information S1). A self-consistent description of the coupled electron-wave evolution will require future kinetic simulations.

Due to the limitations of single-event observations, the conditions under which electron thermal pressure dominates the current sheet force balance remain uncertain. For instance, in a subsequent crossing of a similar region (Figure S8 in Supporting Information S1), the magnetic field orientation had changed, and the pressure balance was instead dominated by ions, with electron thermal pressure slightly lower than that of ions. This suggests that the electron-dominated configuration may be episodic or sensitive to upstream conditions. A comprehensive statistical survey is therefore required to determine the occurrence rate and controlling parameters of this regime.

Our present work highlights a novel role of plasma wave-driven processes in Martian atmospheric escape, where waves do not directly accelerate particles to escape energies, as described in previous studies (e.g., Ergun et al., 2006; Espley et al., 2004; Fowler et al., 2018; Lundin et al., 2011), but instead contribute to electron heating, thereby sustaining the pressure balance structure of the magnetotail current sheet as a key escape pathway for ionospheric plasma. The generation of magnetosonic waves is modulated by both seasonal variations at Mars and transient solar wind activities (Collinson et al., 2018; Fowler et al., 2018). However, the excitation of whistler and ECH waves requires an anisotropic, beam-like, or shell-like electron velocity distribution, which may frequently arise from the mixing of magnetosheath and ionospheric plasmas within the current sheet (e.g., Xu et al., 2024; Zhang et al., 2025).

Conflict of Interest

The authors declare no conflicts of interest relevant to this study.

Data Availability Statement

MAVEN data used in study is available on NASA Planetary Data System (https://pds-ppi.igpp.ucla.edu/search/default.jsp). Specifically, we have analyzed the following data: (a) L2 MAG data (Connerney, 2024) (available at https://pds-ppi.igpp.ucla.edu/collection/urn:nasa:pds:maven.mag.calibrated:data.pl); (b) MAVEN In Situ Key Parameters (Dunn, 2023) (available at https://pds-ppi.igpp.ucla.edu/collection/urn:nasa:pds:maven.insitu.calibrated:data.kp); (c) L2 SWEA data (Mitchell, 2024) (available at https://pds-ppi.igpp.ucla.edu/bundle/urn:nasa:pds:maven.swea.calibrated); (d) L2 STATIC data (McFadden, 2024) (available at https://pds-ppi.igpp.ucla.edu/bundle/urn:nasa:pds:maven.static.c). BO code is available at https://github.com/hsxie/bo. Data from the BO code (used in Figures 3 and 4, Figures S6 and S7 in Supporting Information S1) are archived in the Zenodo repository (Yu, 2025).

Acknowledgments
We acknowledge the entire MAVEN team for providing data. This work was supported by the National Natural Science Foundation of China Grants 42130204, 42441808, 42188101 and 42274198, the Postdoctoral Fellowship Program of China Postdoctoral Science Foundation GZB20240701 and the open project fund of State Key Laboratory of Lunar and Planetary Sciences No. 002/2024/SKL.

References

Andreone, G., Halekas, J. S., Mitchell, D. L., Mazelle, C., & Gruesbeck, J. (2022). Properties of electron distributions in the Martian space environment. *Journal of Geophysical Research: Space Physics*, *127*(1), e29404. https://doi.org/10.1029/2021JA029404

Angelopoulos, V., Cruce, P., Drozdov, A., Grimes, E. W., Hatzigeorgiu, N., King, D. A., et al. (2019). The space physics environment data analysis system (SPEDAS). *Space Science Reviews*, *215*(1), 9. https://doi.org/10.1007/s11214-018-0576-4

Artemyev, A. V., Angelopoulos, V., Halekas, J. S., Runov, A., Zelenyi, L. M., & McFadden, J. P. (2017). Mars's magnetotail: Nature's current sheet laboratory. *Journal of Geophysical Research: Space Physics*, *122*(5), 5404–5417. https://doi.org/10.1002/2017JA024078

Artemyev, A. V., Angelopoulos, V., & Runov, A. (2016). On the radial force balance in the quiet time magnetotail current sheet. *Journal of Geophysical Research: Space Physics*, *121*(5), 4017–4026. https://doi.org/10.1002/2016JA022480

Artemyev, A. V., Angelopoulos, V., Runov, A., & Petrukovich, A. A. (2019). Global view of current sheet thinning: Plasma pressure gradients and large-scale currents. *Journal of Geophysical Research: Space Physics*, *124*(1), 264–278. https://doi.org/10.1029/2018JA026113

Artemyev, A. V., Petrukovich, A. A., Nakamura, R., & Zelenyi, L. M. (2012). Adiabatic electron heating in the magnetotail current sheet: Cluster observations and analytical models. *Journal of Geophysical Research*, *117*(A6), A06219. https://doi.org/10.1029/2012JA017513

Artemyev, A. V., Vasko, I. Y., Angelopoulos, V., & Runov, A. (2016). Effects of electron pressure anisotropy on current sheet configuration. *Physics of Plasmas*, *23*(9), 092901. https://doi.org/10.1063/1.4961926

Barabash, S., Fedorov, A., Lundin, R., & Sauvaud, J.-A. (2007). Martian atmospheric erosion rates. *Science*, *315*(5811), 501–503. https://doi.org/10.1126/science.1134358

Barabash, S., Fedorov, A., Sauvaud, J. J., Lundin, R., Russell, C. T., Futaana, Y., et al. (2007). The loss of ions from Venus through the plasma wake. *Nature*, *450*(7170), 650–653. https://doi.org/10.1038/nature06434

Baumjohann, W. (1998). Ion and electron heating in the near-Earth magnetotail. *Geophysical Monograph Series*, *105*, 97–102. https://doi.org/10.1029/GM105p0097

Brain, D. A., Bagenal, F., Acuña, M. H., Connerney, J. E. P., Crider, D. H., Mazelle, C., et al. (2002). Observations of low-frequency electromagnetic plasma waves upstream from the Martian shock. *Journal of Geophysical Research*, *107*(A6), 1076. https://doi.org/10.1029/2000JA000416

Chaston, C. C., Bonnell, J. W., & Salem, C. (2014). Heating of the plasma sheet by broadband electromagnetic waves. *Geophysical Research Letters*, *41*(23), 8185–8192. https://doi.org/10.1002/2014GL062116

Collinson, G., Wilson, L. B., Omidi, N., Sibeck, D., Espley, J., Fowler, C. M., et al. (2018). Solar wind induced waves in the skies of Mars: Ionospheric compression, energization, and escape resulting from the impact of ultralow frequency magnetosonic waves generated upstream of the Martian bow shock. *Journal of Geophysical Research: Space Physics*, *123*(9), 7241–7256. https://doi.org/10.1029/2018JA025414

Connerney, J. E. P. (2024). MAVEN MAG calibrated data bundle [Dataset]. *NASA Planetary Data System*. https://doi.org/10.17189/1414178

Connerney, J. E. P., Espley, J., Lawton, P., Murphy, S., Odom, J., Oliversen, R., & Sheppard, D. (2015). The MAVEN magnetic field investigation. *Space Science Reviews*, *195*(1–4), 257–291. https://doi.org/10.1007/s11214-015-0169-4

DiBraccio, G. A., Espley, J. R., Gruesbeck, J. R., Connerney, J. E. P., Brain, D. A., Halekas, J. S., et al. (2015). Magnetotail dynamics at Mars: Initial MAVEN observations. *Geophysical Research Letters*, *42*(21), 8828–8837. https://doi.org/10.1002/2015GL065248

Dubinin, E., & Fraenz, M. (2015). Magnetotails of Mars and Venus. In A. Keiling, C. M. Jackman, & P. A. Delamere (Eds.), *Magnetotails in the solar system* (Vol. 207, pp. 34–59). https://doi.org/10.1002/9781118842324.ch3

Dubinin, E., Fraenz, M., Pätzold, M., McFadden, J., Halekas, J. S., DiBraccio, G. A., et al. (2017). The effect of solar wind variations on the escape of oxygen ions from Mars through different channels: MAVEN observations. *Journal of Geophysical Research: Space Physics*, *122*(11), 11285–11301. https://doi.org/10.1002/2017JA024741

Dubinin, E., Modolo, R., Fraenz, M., Päetzold, M., Woch, J., Chai, L., et al. (2019). The induced magnetosphere of Mars: Asymmetrical topology of the magnetic field lines. *Geophysical Research Letters*, *46*(22), 12722–12730. https://doi.org/10.1029/2019GL084387

Dunn, P. A. (2023). MAVEN in situ key parameters data collection [Dataset]. *NASA Planetary Data System*. https://doi.org/10.17189/mhyy-4168

Ergun, R. E., Andersson, L., Peterson, W. K., Brain, D., Delory, G. T., Mitchell, D. L., et al. (2006). Role of plasma waves in Mars' atmospheric loss. *Geophysical Research Letters*, *33*(14), L14103. https://doi.org/10.1029/2006GL025785

Espley, J. R., Cloutier, P. A., Brain, D. A., Crider, D. H., & AcuñA, M. H. (2004). Observations of low-frequency magnetic oscillations in the Martian magnetosheath, magnetic pileup region, and tail. *Journal of Geophysical Research*, *109*(A7), A07213. https://doi.org/10.1029/2003JA010193

Fedorov, A., Barabash, S., Sauvaud, J. A., Futaana, Y., Zhang, T. L., Lundin, R., & Ferrier, C. (2011). Measurements of the ion escape rates from Venus for solar minimum. *Journal of Geophysical Research*, *116*(A7), A07220. https://doi.org/10.1029/2011JA016427

Fedorov, A., Ferrier, C., Sauvaud, J. A., Barabash, S., Zhang, T. L., Mazelle, C., et al. (2008). Comparative analysis of Venus and Mars magnetotails. *Planetary and Space Science*, *56*(6), 812–817. https://doi.org/10.1016/j.pss.2007.12.012

Fowler, C. M., Agapitov, O. V., Xu, S., Mitchell, D. L., Andersson, L., Artemyev, A., et al. (2020). Localized heating of the Martian topside ionosphere through the combined effects of magnetic pumping by large-scale magnetosonic waves and pitch angle diffusion by whistler waves. *Geophysical Research Letters*, *47*(5), e86408. https://doi.org/10.1029/2019GL086408

Fowler, C. M., Andersson, L., Ergun, R. E., Harada, Y., Hara, T., Collinson, G., et al. (2018). MAVEN observations of solar wind-driven magnetosonic waves heating the Martian dayside ionosphere. *Journal of Geophysical Research: Space Physics*, *123*(5), 4129–4149. https://doi.org/10.1029/2018JA025208

Fowler, C. M., Hanley, K. G., McFadden, J. P., Chaston, C. C., Bonnell, J. W., Halekas, J. S., et al. (2021). MAVEN observations of low frequency steepened magnetosonic waves and associated heating of the Martian nightside ionosphere. *Journal of Geophysical Research: Space Physics*, *126*(10), e29615. https://doi.org/10.1029/2021JA029615

Fowler, C. M., McFadden, J., Hanley, K. G., Mitchell, D. L., Curry, S., & Jakosky, B. (2022). In-situ measurements of ion density in the Martian ionosphere: Underlying structure and variability observed by the MAVEN-STATIC instrument. *Journal of Geophysical Research: Space Physics*, *127*(8), e30352. https://doi.org/10.1029/2022JA030352

Fox, J. L., Brannon, J. F., & Porter, H. S. (1993). Upper limits to the nightside ionosphere of Mars. *Geophysical Research Letters*, *20*(13), 1339–1342. https://doi.org/10.1029/93GL01349

Halekas, J. S., Brain, D. A., Lillis, R. J., Fillingim, M. O., Mitchell, D. L., & Lin, R. P. (2006). Current sheets at low altitudes in the Martian magnetotail. *Geophysical Research Letters*, *33*(13), L13101. https://doi.org/10.1029/2006GL026229

Halekas, J. S., Brain, D. A., Lin, R. P., Luhmann, J. G., & Mitchell, D. L. (2008). Distribution and variability of accelerated electrons at Mars. *Advances in Space Research*, *41*(9), 1347–1352. https://doi.org/10.1016/j.asr.2007.01.034

Halekas, J. S., Shaver, S., Azari, A. R., Fowler, C. M., Ma, Y., Xu, S., et al. (2023). The day the solar wind disappeared at Mars. *Journal of Geophysical Research: Space Physics*, *128*(12), e2023JA031935. https://doi.org/10.1029/2023JA031935

Harada, Y., Halekas, J. S., McFadden, J. P., Mitchell, D. L., Mazelle, C., Connerney, J. E. P., et al. (2015). Magnetic reconnection in the near-Mars magnetotail: MAVEN observations. *Geophysical Research Letters*, *42*(21), 8838–8845. https://doi.org/10.1002/2015GL065004

Harris, E. G. (1962). On a plasma sheath separating regions of oppositely directed magnetic field. *Il Nuovo Cimento - B*, *23*(1), 115–121. https://doi.org/10.1007/BF02733547

Ieda, A., Machida, S., Mukai, T., Saito, Y., Yamamoto, T., Nishida, A., et al. (1998). Statistical analysis of the plasmoid evolution with Geotail observations. *Journal of Geophysical Research*, *103*(A3), 4453–4466. https://doi.org/10.1029/97JA03240

Jakosky, B. M., Grebowsky, J. M., Luhmann, J. G., Connerney, J., Eparvier, F., Ergun, R., et al. (2015). MAVEN observations of the response of Mars to an interplanetary coronal mass ejection. *Science*, *350*(6261), 0210. https://doi.org/10.1126/science.aad0210

Jakosky, B. M., Lin, R. P., Grebowsky, J. M., Luhmann, J. G., Mitchell, D. F., Beutelschies, G., et al. (2015). The Mars atmosphere and volatile evolution (MAVEN) mission. *Space Science Reviews*, *195*(1–4), 3–48. https://doi.org/10.1007/s11214-015-0139-x

Li, X. Z., Rong, Z. J., Fraenz, M., Zhang, C., Klinger, L., Shi, Z., et al. (2023). Two types of Martian magnetotail current sheets: MAVEN observations of ion composition. *Geophysical Research Letters*, *50*(2), e2022GL102630. https://doi.org/10.1029/2022GL102630

Liu, K., Gary, S. P., & Winske, D. (2011). Excitation of magnetosonic waves in the terrestrial magnetosphere: Particle-in-cell simulations. *Journal of Geophysical Research*, *116*(A7), A07212. https://doi.org/10.1029/2010JA016372

Lundin, R., Barabash, S., Dubinin, E., Winningham, D., & Yamauchi, M. (2011). Low-altitude acceleration of ionospheric ions at Mars. *Geophysical Research Letters*, *38*(8), L08108. https://doi.org/10.1029/2011GL047064

McFadden, J. P. (2024). MAVEN STATIC calibrated data bundle [Dataset]. *NASA Planetary Data System*. https://doi.org/10.17189/1517741

McFadden, J. P., Kortmann, O., Curtis, D., Dalton, G., Johnson, G., Abiad, R., et al. (2015). MAVEN suprathermal and thermal ion compostion (STATIC) instrument. *Space Science Reviews*, *195*(1–4), 199–256. https://doi.org/10.1007/s11214-015-0175-6

Mitchell, D. L. (2024). MAVEN SWEA calibrated data bundle [Dataset]. *NASA Planetary Data System*. https://doi.org/10.17189/7cx9-xy68

Mitchell, D. L., Mazelle, C., Sauvaud, J. A., Thocaven, J. J., Rouzaud, J., Fedorov, A., et al. (2016). The MAVEN solar wind electron analyzer. *Space Science Reviews*, *200*(1–4), 495–528. https://doi.org/10.1007/s11214-015-0232-1

Nilsson, H., Zhang, Q., Stenberg Wieser, G., Holmström, M., Barabash, S., Futaana, Y., et al. (2023). Solar cycle variation of ion escape from Mars. *Icarus*, *393*, 114610. https://doi.org/10.1016/j.icarus.2021.114610

Núñez, M. (2020). Transmission of magnetosonic waves through current-vortex sheets. *European Journal of Mechanics - B: Fluids*, *79*, 472–479. https://doi.org/10.1016/j.euromechflu.2019.08.009

Robinson, P. A. (1989). New contributions to transit-time damping in multidimensional systems. *Physics of Fluids B*, *1*(3), 490–498. https://doi.org/10.1063/1.859164

Robinson, P. A. (1991). Transit-time damping and the arrest of wave collapse. *Physics of Fluids B: Plasma Physics*, *3*(3), 545–554. https://doi.org/10.1063/1.859905

Ruhunusiri, S., Halekas, J. S., Connerney, J. E. P., Espley, J. R., McFadden, J. P., Larson, D. E., et al. (2015). Low-frequency waves in the Martian magnetosphere and their response to upstream solar wind driving conditions. *Geophysical Research Letters*, *42*(21), 8917–8924. https://doi.org/10.1002/2015GL064968

Seki, K., Elphic, R. C., Hirahara, M., Terasawa, T., & Mukai, T. (2001). On atmospheric loss of oxygen ions from Earth through magnetospheric processes. *Science*, *291*(5510), 1939–1941. https://doi.org/10.1126/science.1058913

Shen, H.-W., Halekas, J. S., Curry, S. M., Zhang, C., Wen, Y., & Espley, J. R. (2025). Statistical analysis of ion properties in the Martian magnetosheath based on MAVEN observations: A comparison of core and total ion populations. *The Astrophysical Journal*, *990*(2), 115. https://doi.org/10.3847/1538-4357/adf6a9

Shklyar, D. R. (2017). Energy transfer from lower energy to higher-energy electrons mediated by whistler waves in the radiation belts. *Journal of Geophysical Research (Space Physics)*, *122*(1), 640–655. https://doi.org/10.1002/2016JA023263

Short, R. W., & Simon, A. (1998). Landau damping and transit-time damping of localized plasma waves in general geometries. *Physics of Plasmas*, *5*(12), 4124–4133. https://doi.org/10.1063/1.873146

Sonnerup, B. U. Ö., & Scheible, M. (1998). Minimum and maximum variance analysis. *ISSI Scientific Reports Series*, *1*, 185–220.

Stix, T. H. (1992). *Waves in plasmas*. American Institute of Physics. Melville, NY.

Su, Z., Liu, N., Gao, Z., Wang, B., Zheng, H., Wang, Y., & Wang, S. (2020). Rapid Landau heating of Martian topside ionospheric electrons by large-amplitude magnetosonic waves. *Geophysical Research Letters*, *47*(20), e90190. https://doi.org/10.1029/2020GL090190

Su, Z., Wang, Y., Zhang, T., Wu, Z., Cheng, L., Zou, Z., et al. (2023). Unusual Martian foreshock waves triggered by a solar wind stream interaction region. *The Astrophysical Journal Letters*, *947*(2), L33. https://doi.org/10.3847/2041-8213/accb9f

Summers, D., Ni, B., & Meredith, N. P. (2007). Timescales for radiation belt electron acceleration and loss due to resonant wave-particle interactions: 2. Evaluation for VLF chorus, ELF hiss, and electromagnetic ion cyclotron waves. *Journal of Geophysical Research*, *112*(A4), A04207. https://doi.org/10.1029/2006JA011993

Sundkvist, D., Vaivads, A., Bogdanova, Y. V., Krasnoselskikh, V. V., Fazakerley, A., & Décréau, P. M. E. (2006). Shell-instability generated waves by low energy electrons on converging magnetic field lines. *Geophysical Research Letters*, *33*(3), L03103. https://doi.org/10.1029/2005GL024388

Tataronis, J. A., & Crawford, F. W. (1970). Cyclotron harmonic wave propagation and instabilities: I. perpendicular propagation. *Journal of Plasma Physics*, *4*(2), 231–248. https://doi.org/10.1017/S0022377800004979

Tsurutani, B. T., & Smith, E. J. (1984). Magnetosonic waves adjacent to the plasma sheet in the distant magnetotail: ISEE-3. *Geophysical Research Letters*, *11*(4), 331–334. https://doi.org/10.1029/GL011i004p00331

Umeda, T., Ashour-Abdalla, M., Schriver, D., Richard, R. L., & Coroniti, F. V. (2007). Particle-in-cell simulation of Maxwellian ring velocity distribution. *Journal of Geophysical Research*, *112*(A4), A04212. https://doi.org/10.1029/2006JA012124

Umeda, T., Matsukiyo, S., Amano, T., & Miyoshi, Y. (2012). A numerical electromagnetic linear dispersion relation for Maxwellian ring-beam velocity distributions. *Physics of Plasmas*, *19*(7), 072107. https://doi.org/10.1063/1.4736848

Wen, Y., Rong, Z., Nilsson, H., Zhang, C., Shen, H.-W., & Gao, J. (2025). Statistical investigations of the radial IMF component impact on the magnetotail current sheet structure of Mars: MAVEN observations. *ESS Open Archive*. https://doi.org/10.22541/essoar.175767465.50711331/v1

Wu, Z., Su, Z., Zheng, H., & Wang, Y. (2023). Filtering of magnetosonic waves by mesoscale plasmaspheric density interfaces. *Geophysical Research Letters*, *50*(11), e2023GL103590. https://doi.org/10.1029/2023GL103590

Xie, H.-S. (2019). BO: A unified tool for plasma waves and instabilities analysis. *Computer Physics Communications*, *244*, 343–371. https://doi.org/10.1016/j.cpc.2019.06.014

Xie, H.-S., & Xiao, Y. (2016). PDRK: A general kinetic dispersion relation solver for magnetized plasma. *Plasma Science and Technology*, *18*(2), 97–107. https://doi.org/10.1088/1009-0630/18/2/01

Xu, S., Mitchell, D. L., Halekas, J. S., McFadden, J. P., Fowler, C. M., Hanley, K., et al. (2024). Electron energization by ion density enhancement in the Martian magnetotail—Maven observations. *The Astrophysical Journal*, *975*(2), 246. https://doi.org/10.3847/1538-4357/ad863e

Yu, L. (2025). Hot plasma wave dispersion relations inside and outside the current sheet [Dataset]. *Zenodo*. https://doi.org/10.5281/zenodo.17188626

Zelenyi, L., Malova, H., Grigorenko, E., Popov, V., & Delcourt, D. (2019). Current sheets in planetary magnetospheres. *Plasma Physics and Controlled Fusion*, *61*(5), 054002. https://doi.org/10.1088/1361-6587/aafbbf

Zelenyi, L. M., Malova, H. V., Leonenko, M. V., Grigorenko, E. E., & Popov, V. Y. (2022). Equilibrium configurations of super-thin current sheets in space plasma: Characteristic scaling of multilayer structures. *Journal of Geophysical Research: Space Physics*, *127*(11), e2022JA030881. https://doi.org/10.1029/2022JA030881

Zhang, C., Dong, C., Zhou, H., Deca, J., Xu, S., Harada, Y., et al. (2025). Observational characteristics of electron distributions in the Martian induced magnetotail. *Geophysical Research Letters*, *52*(7), 2024GL113030. https://doi.org/10.1029/2024GL113030

Zhang, C., Rong, Z., Li, X., Fränz, M., Nilsson, H., Jarvinen, R., et al. (2024). The energetic oxygen ion beams in the Martian magnetotail current sheets: Hints from the comparisons between two types of current sheets. *Geophysical Research Letters*, *51*(5), e2023GL107190. https://doi.org/10.1029/2023GL107190